ARL-TR-9939 ● July 2024

Flow Field Characterization of a Generic High-Speed Projectile Configuration

by James DeSpirito, Royce Pokela, and Rajan Kumar

NOTICES

Disclaimers

ARL-TR-9939 ● JULY 2024

Flow Field Characterization of a Generic High-Speed Projectile Configuration

James DeSpirito
DEVCOM Army Research Laboratory

Royce Pokela and Rajan Kumar
Florida Center for Advanced Aero-Propulsion, FAMU-FSU College of Engineering

REPORT DOCUMENTATION PAGE

1. REPORT DATE	2. REPORT TYPE	3. DATES COVERED START DATE	END DATE
July 2024	Technical Report	7/31/2022	1/04/2024

4. TITLE AND SUBTITLE
Flow Field Characterization of a Generic High-Speed Projectile Configuration

5a. CONTRACT NUMBER	5b. GRANT NUMBER	5c. PROGRAM ELEMENT NUMBER
5d. PROJECT NUMBER	**5e. TASK NUMBER**	**5f. WORK UNIT NUMBER**

6. AUTHOR(S)
James DeSpirito, Royce Pokela, and Rajan Kumar

7. PERFORMING ORGANIZATION NAME(S) AND ADDRESS(ES)	8. PERFORMING ORGANIZATION REPORT NUMBER
DEVCOM Army Research Laboratory ATTN: FCDD-RLA-WD Aberdeen Proving Ground, MD 21005	ARL-TR-9939

9. SPONSORING/MONITORING AGENCY NAME(S) AND ADDRESS(ES)	10. SPONSOR/MONITOR'S ACRONYM(S)	11. SPONSOR/MONITOR'S REPORT NUMBER(S)

12. DISTRIBUTION/AVAILABILITY STATEMENT
DISTRIBUTION STATEMENT A. Approved for public release: distribution unlimited.

13. SUPPLEMENTARY NOTES

14. ABSTRACT
A combined experimental and numerical study was conducted on a generic projectile configuration with four high-sweep, low-aspect-ratio fins. The investigation expands on previous investigations of this configuration comparing high-fidelity computational fluid dynamic predictions of flow field structures to wind tunnel flow diagnostics including high-speed shadowgraphy, oil-flow visualization, and fast-response pressure-sensitive paint over the Mach number range of 0.7 to 4.0. The predicted vortex structures compared very well with those observed on the wind tunnel model. The predicted surface streak lines and pressure distribution also compared well with the wind tunnel results. Comparison of predicted and wind tunnel surface pressure distributions shows that the simulations tended to overpredict the surface pressure at most locations, primarily on the leeward surfaces of the fins. Turbulence model and rotation-correction modifications showed little effect on the surface pressure distribution except on the leeward surface of the lower fin, where using a rotation-correction modification improved the comparison with the wind tunnel result.

15. SUBJECT TERMS
shock-boundary layer interaction, vortex interactions, high-speed flight, computational fluid dynamics, wind tunnel, shadowgraphy, pressure-sensitive paint, Weapons Sciences

16. SECURITY CLASSIFICATION OF: a. REPORT	b. ABSTRACT	C. THIS PAGE	17. LIMITATION OF ABSTRACT	18. NUMBER OF PAGES
UNCLASSIFIED	UNCLASSIFIED	UNCLASSIFIED	UU	39

19a. NAME OF RESPONSIBLE PERSON	19b. PHONE NUMBER *(Include area code)*
James DeSpirito	(410) 306-0778

STANDARD FORM 298 (REV. 5/2020)
Prescribed by ANSI Std. Z39.18

Contents

List of Figures

List of Tables

Acknowledgments

The authors thank Joseph D Vasile, US Army Combat Capabilities Development Command (DEVCOM) Army Research Laboratory (ARL), for providing the original computational mesh that was used in previous studies. This study forms a part of a Cooperative Research and Development Agreement (CRADA #17-031-J004) established between ARL and Florida A&M University–Florida State University College of Engineering. This work was supported in part by a grant of high-performance computing time from the US DOD High-Performance Computing Modernization Program.

1. Introduction

The development of high-speed flight vehicles, such as missiles and projectiles, requires detailed experimental and numerical investigations to generate an aerodynamic database and characterize the flow physics associated with complex geometries. Even for a generic configuration, this can involve significant three-dimensionality with crossflow separation, shock-boundary layer interactions (SBLIs), fluid–structure interactions, and unsteady wake–plume interactions. Additionally, the flow field experienced by an aerodynamic body will vary across an extended Mach range, including nonlinear effects at transonic speeds and compressibility effects at high supersonic or hypersonic speeds. While there is a large selection of advanced computational tools specifically developed to assist in the design of complex aerospace systems, limitations remain that lead to the continued use of experimental investigations in parallel to provide validation data and better understand the flow physics.

In the present study, a comprehensive experimental and numerical investigation was carried out for a symmetric slender body configuration with four low-aspect-ratio fins under a cooperative agreement between the US Army Combat Capabilities Development Command (DEVCOM) Army Research Laboratory (ARL) and Florida State University (FSU). This work is a continuation of earlier studies to characterize the aerodynamics and associated flow physics on this generic flight body.[1,2] The configuration of interest is a generic slender body with four high-sweep, low-aspect-ratio fins, optimized for high-speed, long-range flight.[3] Previous computational fluid dynamics (CFD) characterization of this configuration[4] indicated that the roll orientation of the model had a notable effect on the lift generation and longitudinal stability. The comparison of inviscid and viscous CFD predictions highlighted the viscous effects on the fin effectiveness. Additional vortex structures were observed in the viscous computations and these likely explained the differences in pitching moment prediction between the inviscid and viscous solvers at moderate angles of incidence. At the maximum angle of incidence investigated in this study, $\alpha_t = 12°$, the primary vortex structures are formed on the fins, without the effects of asymmetric body vortices from smooth-surface separation. The primary vortex structures resemble delta wing vortices, but with added complexity of windward and leeward effects due to missile roll angle. SBLI effects are also present as the fin-generated shocks interact with the boundary layer.

In the previous studies,[1,2] the emphasis was on the aerodynamic characterization of the projectile, that is, the determination of the aerodynamic coefficients. The computational mesh was designed primarily with that in mind and the CFD predictions compared well with the wind tunnel (WT) values, including lateral loads developed in asymmetric roll orientations. This mesh was adequate to obtain the aerodynamic coefficients while still resolving the primary vortex and shock structures. The CFD simulations were also performed on the full-scale model,[3] not the one-fifth-scale WT model used in the experiments,[1,2] and captured the primary vortex and shock structures.[2,4] Pokela et al.[5] continued the experimental investigation of this configuration using pressure-sensitive paint (PSP) to acquire the surface pressure distribution on a slightly larger, one-quarter-scale model. These measurements were paired with surface oil-flow and shadowgraph visualization to obtain information on the overall flow field, including the development of the flow structures with angle of incidence. The main objectives of that study were to qualify the PSP measurements, observe the flow feature development with angle of incidence, and quantify the effects of various flow features that occur on the model. The PSP provided pressure contours on both the model's cylindrical body and the fins together, and features compared well with those observed in oil-flow results.

The goal of the present study is to further evaluate the flow field to better understand the flow physics and quantify their effect on the resulting aerodynamic force and moment coefficients. The original computational mesh[1,2,4] was scaled down to match the one-fifth-scale WT model to minimize Reynolds number effects. The predicted longitudinal aerodynamic coefficients are first compared to those obtained in the WT. The flow features on the projectile body and fins are then compared to the WT oil-flow and PSP results and predicted off-body flow features are presented. Surface pressure profiles extracted from the WT experiments and the CFD simulations are then compared at two angles of incidence to quantify the prediction accuracy. Finally, the effect of turbulence model is presented.

2. Experimental Approach

2.1 Test Model

The experimental configuration in this study was a generic, axisymmetric ogive-cylinder body with four high-sweep, low-aspect-ratio fins (Fig. 1). Two WT test models were investigated over the course of the study. The first was a one-fifth-scale model used in the collection of aerodynamic load, shadowgraph, and oil-flow data.[1,2] This model had a 21.0-mm (0.83-inch) diameter, D, and a slenderness ratio of 10. The second model was scaled up to one-quarter scale, that is, $D = 26.2$ mm (1.033 inch), in the PSP study.[5] The generic features of both models are shown in Fig. 1, including the five static pressure ports (three on top, two on starboard side) in the one-quarter-scale model that were used for in-situ calibration of the PSP in that study. The model featured a $3D$-long, blunt von Kármán ogive nose with a $0.1D$ nose radius. The root fin chord of the fins was $6D$, the tip fin chord was $2.2D$, and the tip-to-tip fin span was $1.935D$. A transition strip was located $1D$ downstream of the nose to artificially transition the boundary layer for simulation of a larger-scale model. The strip consisted of a 1-mm strip of silicon carbide particles in the one-fifth-scale model while the strip was machined on the surface in the one-quarter-scale model. Screw holes were filled with repair putty that was dried and smoothed before testing. Additional information on the aerodynamics of this configuration can be obtained in Vasile and Sahu.[4]

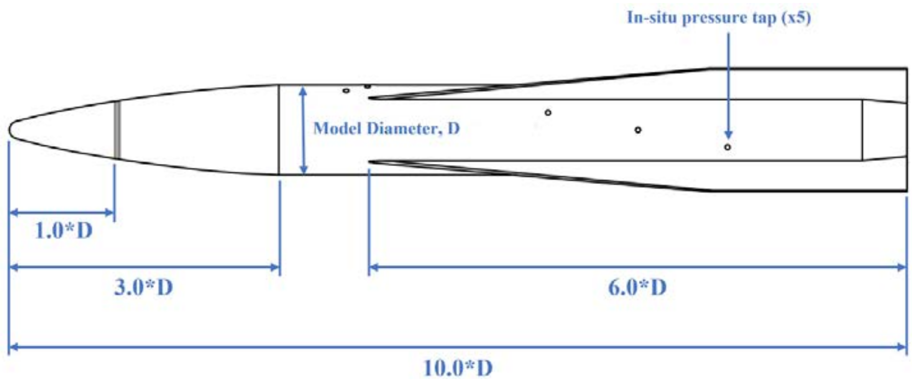

Fig. 1 Geometric detail of WT model, top view, $\phi = 0°$

2.2 Wind Tunnel Facility

The FSU polysonic wind tunnel (PSWT) (Fig. 2) is a blowdown WT that operates in the subsonic, transonic, and supersonic regimes, up to Mach 5. Models can be sting, floor, or wall mounted within a 12- × 12- × 24-inch test section for subsonic and supersonic testing, or a 12- × 12- × 48-inch test section with slotted walls for transonic testing. Subsonic and transonic Mach numbers are achieved through back pressure or plenum pressure variation and range continuously from Mach 0.2 to Mach 1.2. Supersonic Mach numbers are achieved using fixed area ratio nozzle blocks. With the use of an acoustically treated stagnation chamber, conditioning screens, and a flow straightener, the tunnel produces excellent flow quality. Both root-mean-squared (RMS) pressure fluctuations and turbulence intensity are less than 0.2% at supersonic speeds. Flow angularity in both the pitch and yaw plane are less than 0.2°.

The PSWT has an arc sector with a variable roll mechanism that has precise control during WT runs, allowing for forces and moments to be measured through a range of pitch (–10° to 12°) and roll (–180° to 180°) angles. Force balances are sting mounted to the arc sector and roll mechanism with room for pressure tubing to be routed for base pressure measurements. Additional information about the tunnel can be found in Van Every et al.[6]

High-speed shadowgraphy was carried out to help visualize flow features including body and fin shocks, SBLIs and the trajectory of forebody vortices. The shadowgraph setup is a conventional Z-type arrangement using a Phantom camera, a high-speed LED circuit, and a delay generator. Each test was captured at 200 Hz. The images were postprocessed to improve signal-to-noise ratio. Intensity RMS analysis on a total of 100 frames per test was conducted to increase definition of the flow features produced during the tests.

Surface oil-flow visualization was obtained to capture and observe the development of surface flow features. The mixture used was made with fluorescent powder and mineral oil, which was illuminated with intense UV light. High-resolution video was obtained using a Prosilica GT camera and a long-pass light filter. The model was painted in a quadrant pattern with two separate colors to track streak lines across the model. Oil-flow visualization was conducted at $\alpha = 0°$ and $\alpha = 12°$ at Mach 0.7, 1.1, 2, and 4. At transonic conditions, the model was already pitched at the start of the test. At supersonic conditions, the model was pitched after the tunnel fully achieved conditions due to higher start-up loads.

Fig. 2 FSU polysonic WT

High-speed pressure-sensitive paint was used to obtain the surface pressure distribution on the model.[5] PSP techniques use paints that include oxygen-sensitive luminophores that, when excited, vary in emission intensity dependent on the local pressure. The paint in this investigation was a fast-response (≈8 kHz) formulation that utilized a Pt(II) meso-tetra (pentafluorophenyl) porphine (PtTFPP) dye within a titanium dioxide nano-ceramic matrix. The paint mixture was applied to the model cylinder and fins separately to avoid emission interference between the two surfaces. Results between the cylinder and the fins were combined in postprocessing for analysis. The paint was excited using 400-nm UV LED lights.

Multiple lights were used per viewing angle to maintain a relatively even light distribution. Images were recorded using two Phantom v2012 high-speed cameras—one for each viewing window, top and side, at 20,000 fps for 1 s of run time to avoid significant temperature changes during data acquisition. A 610-nm long-pass filter was fixed to the lens of each camera to isolate the paint emission. Images were registered before intensity ratios of wind-off to wind-on images were taken and pressure calibration was applied.

Forces and moments were measured using a 0.5-inch-diameter ARI Mk-XV 6-axis internal strain gage force balance. Maximum loads for normal force, side force, and axial force (at zero moments) were 200, 100, and 50 lbf, respectively. Maximum loads for pitching, yawing, and rolling moments (at zero forces) were 210, 85, and 50 in-lbf, respectively. Prior to testing, each bridge of the force balance was carefully calibrated. Additionally, prior to each individual run, the force balance underwent a "wind-off" run, where the upcoming pitch-and-roll sweep was conducted to obtain the forces and moments produced by the weight of the model and balance, to be removed from the test results in processing. The balance was sting mounted to a pitch-and-roll mechanism to acquire data during pitch-and-roll sweeps. The angle of incidence was varied from $0°$ to $12°$ at the rate of $2°$ per second. The roll orientation of the test model was varied from $-90°$ to $90°$ at the rate of $20°$ per second. Model base pressure was measured using two Kulite fast-response pressure transducers of 0–30 psia pressure range to provide drag corrections that account for the presence of the sting. Each transducer was connected to tubing that was mounted on the sting at the rear of the model. Coefficients were then derived using the force balance data, base pressure measurements, and measured tunnel conditions. Coefficients were derived using the standardized processes described by AIAA.[7]

The uncertainty associated with the force balance is within ±0.1% of the full capacity for each element. The other two factors considered in the uncertainty for the derived coefficients are the dynamic pressure term, q_∞, and the measured model diameter, D, which was measured to ±0.001 inch (model diameter is included in the calculation of the cross-sectional area, S). The dynamic pressure term was derived from static and stagnation pressures measured in the WT. The uncertainty associated with the coefficient of axial force also included the base pressure uncertainty. Uncertainty for the coefficient of drag was dependent on angle of incidence, and therefore calculated at $\alpha_t = 12°$. Estimated derived uncertainty of the aerodynamic coefficients, calculated using the root-sum-square method, are shown in Table 1. Within-test repeatability variation was well below these values. Repeat runs were conducted at Mach 0.7, 1.1, and 2.0. The absolute value of the difference in measurements across interpolated set points were averaged for each run pair and divided by a statistical bias factor. This method used for calculating within-test repeatability for aerodynamic database generation is further described in Houlden et al. and Favaregh et al.[8,9] The resulting standard deviation (σ) values for each aerodynamic coefficient are included in Table 1 as an average between three Mach numbers.

Table 1 Measurement uncertainties

Coefficient	Derived uncertainty	Repeatability (σ)
C_N	0.019	0.005
C_{PM}	0.019	0.006
C_{SF}	0.017	0.002
C_D	0.015	0.005

3. Computational Approach

High-fidelity CFD simulations of the flow field were obtained using the Kestrel software framework developed in the Computational Research and Engineering Acquisition Tools and Environments (CREATE)-Air Vehicles program under the US DOD High-Performance Computing Modernization Program (HPCMP).[10] The Kestrel CFD (KCFD) solver[11] is one of several flow solvers available in the Kestrel framework. KCFD is a cell-centered, finite-volume, unstructured Reynolds-averaged Navier-Stokes (RANS) flow solver for meshes composed of tetrahedral, prismatic, pyramidal, and hexahedral elements. Various exact and approximate Riemann schemes are available to compute the inviscid fluxes at each element face but the HLLE^{++} scheme is the default and was used in this study. The alpha-damping scheme[12] is used to compute the viscous fluxes and the van Leer scheme is used for the viscous flux Jacobian calculations. The Kestrel standard flux limiter was used in this study. Up to second-order temporal accuracy is achieved via a sub-iterative point-implicit time-integration scheme. Kestrel version 12.6.1 was used in this investigation with a Courant–Friedrichs–Lewy-based local time-step approach to advance the flow field to steady state. The walls were modeled as no-slip, adiabatic walls. The outer boundary of the domain was a sphere at 20 body lengths from the projectile center of gravity (c.g.) and was set to the far-field condition, which is a modified Riemann invariant. This method is identical to the “fixed” properties method for supersonic inflow and outflow and applies a characteristic boundary condition for subsonic inflows. For subsonic outflows, static pressure is held constant at the user-specified value while other variables are extrapolated from the domain. Fully turbulent simulations were performed using Menter’s two-equation, k-ω Shear Stress Transport (SST) model.[13,14] The effect of the turbulence model on the predicted solutions was evaluated in a limited study with the addition of the one-equation, Spalart–Allmaras (SA) model.[15] Predictions were also performed using two rotation-correction approaches, one by Dacles-Mariani et al.,[16] labeled SAR and SSTR, and one by Shur et al.,[17] labeled SARC and SSTRC. One benefit of the rotation-correction modifications is to reduce the overprediction of turbulent kinetic energy in the vortex core, thereby reducing overprediction of vortex diffusion.

The computational geometry of the one-fifth-scale model is shown in Fig. 3 with the projectile cruciform fins in the "x" orientation, which is defined here as a roll angle of $\phi = 0°$. All computations in this study were performed with this size model. The side view also shows axial locations where cross-plane flow visualizations were obtained and discussed in Section 4. The mesh was generated using the Capstone mesh generator[18] developed under the CREATE program. A hybrid mesh with triangular cells on the geometry surface, prism layer cells extruded from the surface to capture the boundary layer, and tetrahedral cells in the remainder of the flow field. Mesh symmetry about the longitudinal plane was not controlled as the full domain volume was generated at once. A relatively fine mesh was on the geometry surface (Fig. 4) and therefore in the prism layer region close to the surface. A cylindrical density region encapsulated the near-body and wake region of the flow field (Fig. 5). As shown in the lower image of Fig. 5, the region between the fins was not as finely resolved. While this mesh was adequate to capture the primary flow structures and quantify the aerodynamic coefficients, as confirmed via comparison with WT data,[1,2] it possibly did not adequately maintain vortex intensity with downstream distance, nor capture the secondary vortex structures that might have led to the small discrepancies in moment predictions.

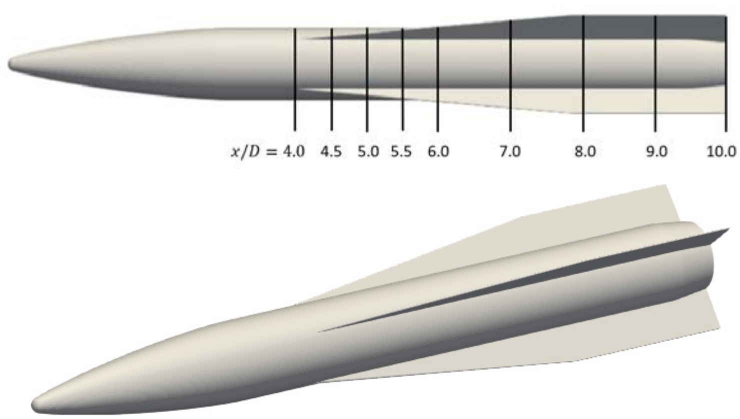

Fig. 3 Port side (top) and angled (bottom) view of computational test model

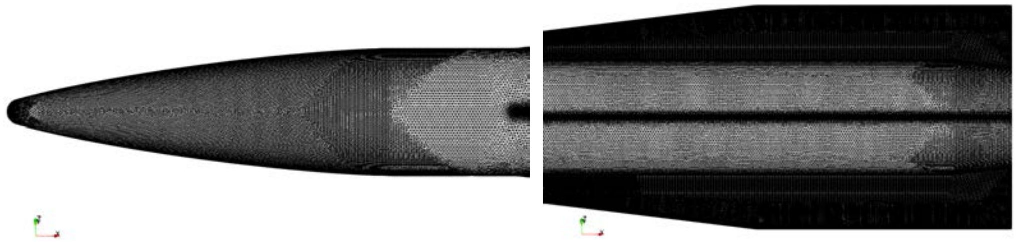

Fig. 4 Computational mesh on model geometry surface: forebody (left) and aftbody (right) with view along the upper port fin span direction

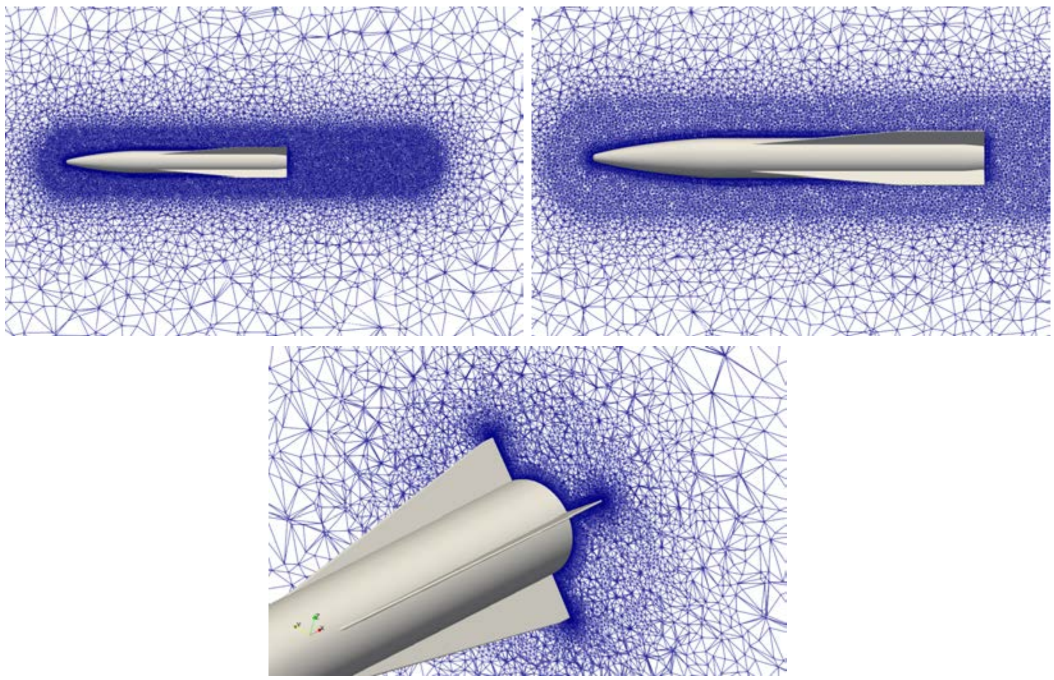

Fig. 5 Computational mesh on longitudinal slice along model geometry axis (top) and axial slice at $x/D = 8.38$ from the nose (bottom)

4. Results and Discussion

Steady-state RANS simulations were performed using the mesh described in Section 3 to characterize the flow field around this generic projectile configuration. Most simulations were performed using Menter's SST turbulence model as our baseline model for the investigation. Two angles of incidence, $\alpha_t = 6°$ and $\alpha_t = 12°$, were investigated. Four Mach numbers, $M = 0.7$, 1.1, 2.0, and 4.0, were investigated at $\alpha_t = 12°$ to compare flow field characteristics to those observed in the WT investigations of Pokela et al.[1,2] The effects of angle of incidence and turbulence model were only performed at $M = 2.0$ to compare to the WT results of Pokela et al.[2,5] The flow conditions used in the computations are shown in Table 2 and are based on the WT conditions. All CFD predictions were performed on a one-fifth-scale computational model. The WT experiments presented in Section 4.1 also used a one-fifth-scale test model, while those experiments presented in Section 4.2 used a one-quarter-scale test model.

Table 2 CFD flow conditions

M_∞	P_{0_∞} (Pa)	P_∞ (Pa)	q_∞ (Pa)	T_{0_∞} (K)	T_∞ (K)	Re/m (m^{-1})
0.7	152,063	109,627	37,601.9	292.3	266.2	19.5×10^6
1.1	151,629	71,016.0	60,150.1	293.4	236.2	23.2×10^6
2.0	205,001	26,200.1	73,360.3	293.8	163.2	25.8×10^6
4.0	837,493	5,515.8	61,777.0	299.0	71.2	36.7×10^6

4.1 Effects of Mach Number

4.1.1 Aerodynamic Coefficients

Previous RANS simulations using another CFD code on the full-scale model[3,4] showed good aerodynamic coefficient comparisons with the WT results.[1,2] Table 3 compares the longitudinal aerodynamic coefficients predicted in the current study using the same one-fifth-scale model in both the WT and CFD at the four Mach numbers and $\alpha_t = 12°$. Both WT- and CFD-derived coefficients show the typical peak near Mach 1 followed by a decreasing trend as Mach number increased. The drag coefficients compare reasonably well, with difference of 11% to 21%. The forebody axial force (projectile base not included [not shown]) compares slightly better at 7.4%–14.1%. The normal force, which consists primarily of the pressure force component, compares very well, with the difference between 1.1% and 2.7%. The prediction of pitching moment is more susceptible to surface separation and vortex development. The pitching moment about the c.g. ($x/D = 6.0$) shows large differences (26%–52%) for Mach 0.7–2.0. At Mach 4.0, the vehicle is now unstable with the center of pressure, $x_{cp} = \mathrm{MRP} - C_{PM}/C_N$, now forward of the c.g. The differences in predicted and experimental pitching moments are exaggerated because the static margin ($x_{cp} - x_{cg}$) is very small (0.065–0.226 cal.) when MRP=x_{cg}. If the MRP is transferred to the nose ($x = 0$), the predicted pitching moments are now within 0.24%–3.7%. However, this illustrates the need for improved computational accuracy to predict pitching moment for highly maneuverable configurations with small static margin.

Table 3 Comparison of aerodynamic coefficients from WT and CFD ($\alpha_t = 12°$)

Mach	WT				CFD			
	C_D	C_N	$C_{PM_{cg}}$	$C_{PM_{nose}}$	C_D	C_N	$C_{PM_{cg}}$	$C_{PM_{nose}}$
0.7	0.73	2.56	–0.579	–15.96	0.83	2.51	–0.294	–15.37
1.1	0.86	2.74	–0.843	–17.29	1.09	2.69	–0.623	–16.73
2.0	0.82	2.70	–0.425	–16.61	0.97	2.67	–0.205	–16.22
4.0	0.63	2.20	–0.144	–13.35	0.72	2.26	0.186	–13.38

4.1.2 Flow Features

The WT experiments included high-speed shadowgraph video and surface oil-flow visualization runs to identify the surface flow features.[1,2] Images of the oil flow overlaid on processed shadowgraphs are shown on left side of Fig. 6 to visualize how the surface flow features and surrounding flow fields develop. The oil-flow liquid was a mixture of mineral oil and fluorescent powder with the model painted with the oil in a quadrant pattern with two separate colors to help track streak lines across the model. The four Mach numbers are shown with the model in the "x" ($\phi = 0°$) orientation and at $\alpha_t = 12°$. No shocks were visible on the model at $M = 0.7$, but at $M = 1.1$, the highly unsteady leading shock, as well as additional body shocks are highlighted by the RMS image processing. At $M = 0.7$, the fin tip vortices originating on the leeward fins are very well defined. However, with an increase in Mach number, these vortices appear to break down and are no longer visible at Mach 4. (It is shown in Fig. 7 that at $M = 4.0$, the fin-tip vortices are closer to the body and of less intensity, likely making them difficult to observe in the shadowgraph.) Additionally, with an increase in Mach number, there is a growth of vortex flow developing on the top of the cylinder. The primary flow features marked on the WT shadowgraphs were based on these images with some preliminary CFD flow visualization.[4] Flow visualizations from the current CFD study will help identify these flow features.

Corresponding CFD flow visualization images are shown on the right side of Fig. 6, which show projectile surface flow patterns and numerical Schlieren ($| \nabla\rho |$) visualizing the shock structures (if present) on the longitudinal symmetry plane of the projectile. These images were generated using the ParaView[19] open-source flow visualization software. The surface flow patterns are visualized using the line integral convolution (LIC) method to visualize the skin friction coefficient vector. The fin-tip vortices observed in the WT shadowgraph cannot be observed in the CFD image because only the slice through the flow field along the projectile axis is shown. However, these can be observed in other visualizations. The shocks at the supersonic Mach numbers compare well to the experiments, though they are diffused as the mesh resolution decreases away from the body (with minimal or no effect on the aerodynamic loads). The surface flow features compare qualitatively with those observed in the experiment and a more detailed comparison of the Mach 2 case is presented later in this section.

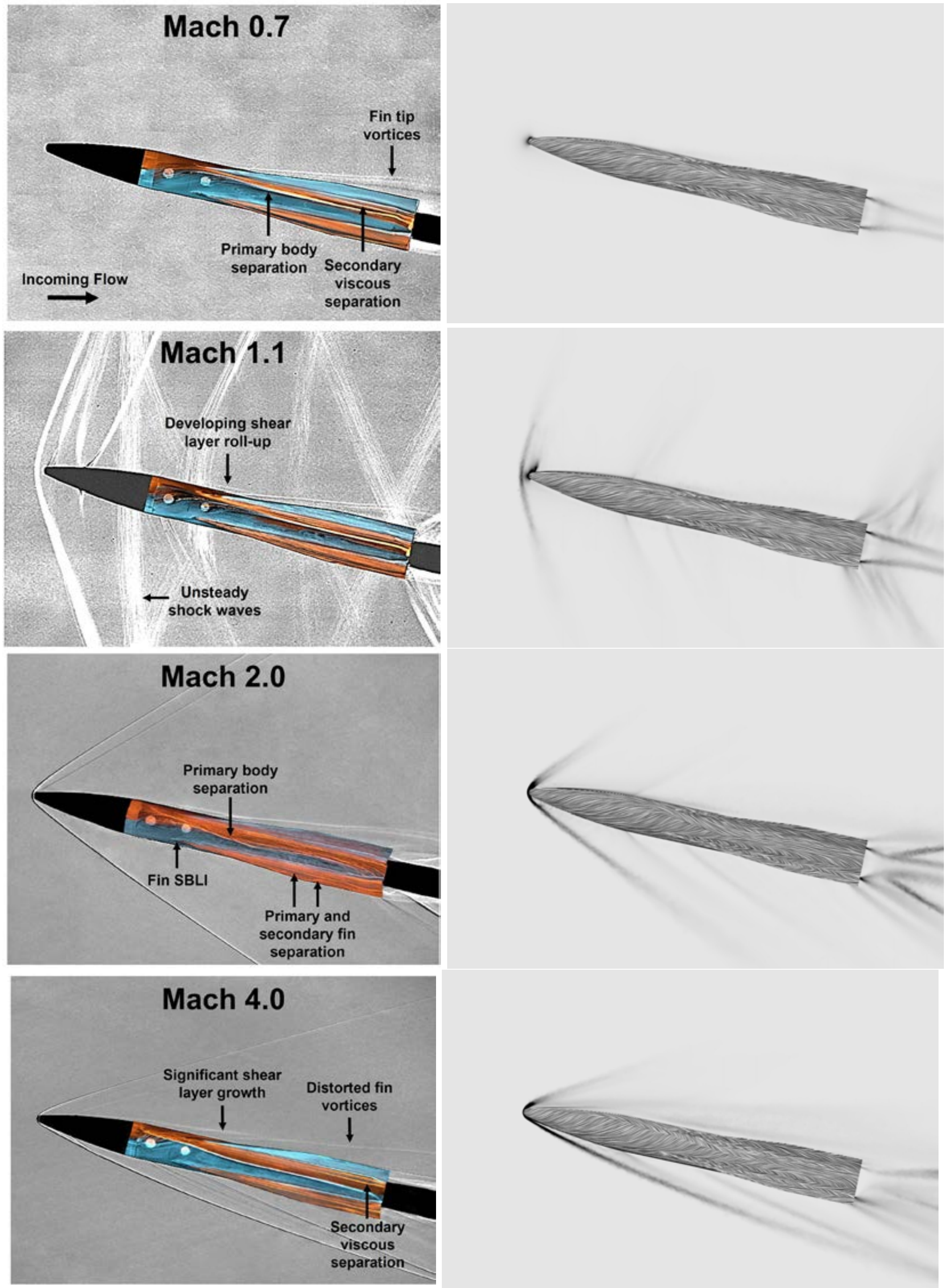

Fig. 6 (Left) Processed shadowgraph images with additional oil flow overlaid to highlight surface flow features, taken at $\alpha_t = 12^\circ$ and $\phi = 0^\circ$; (right) numerical Schlieren of CFD flow field on longitudinal slice along model axis and LIC representation of skin friction coefficient vector on model surface

The predicted vortex structures are shown in Fig. 7, visualized using isosurfaces of scaled Q-criterion (value = 0.5) with a translucency of 0.35. In the scaled Q-criterion, the original definition is divided by the strain tensor, which further removes the effects of the strain-dominated vorticity developed in the boundary layer. The isosurfaces are colored by normalized helicity to indicate rotation direction and relative intensity. In the present coordinate system (x rearward, z up), positive vortex rotation is clockwise as viewed from the front. Also shown in Fig. 7 are two axial cut planes (clipped to a region close to the body) visualizing the flow field via the LIC method on the velocity vector. The cut planes are at $x/D = 8.38$ and $x/D = 10.0$, the latter being at the base of the projectile. These cut-plane flow visualizations help interpret the flow structures and their separation and reattachment location on the projectile surface. The vortex structures are generally similar between the Mach 0.7 and 1.1 flows with the primary upper fin vortices emanating from the leading-edge fin-body junction and traveling along the fin tip. Smaller vortices are observed near the leeward side of the upper fin root and increase in size at Mach 2 but then decrease again at Mach 4. Similar but larger vortices are observed along the windward side of the upper fin root, again having the largest size at Mach 2. On the lower fins, the primary vortex again emanates from the leading-edge fin-body junction with a secondary vortex closer to the fin tip. This primary vortex moves closer to the body at Mach 2 and 4 with a noted decrease in size at Mach 4 and loss of the clockwise (positive helicity) secondary vortex. A small vortex is also observed at the fin root-body junction. A change is observed at Mach 4, where the symmetric vortices emanating from the body are larger and merge with the upper fin-tip vortices. Pokela et al.[2] analyzed CFD predictions using the same mesh as the current study but with a different flow solver. They observed that the change in the peak normalized vorticity in these vortex structures was relatively small in comparison to significant changes in surface pressure effects. The normalized vorticity dropped substantially at Mach 4 and the vortices showed distorted and compressed structures.

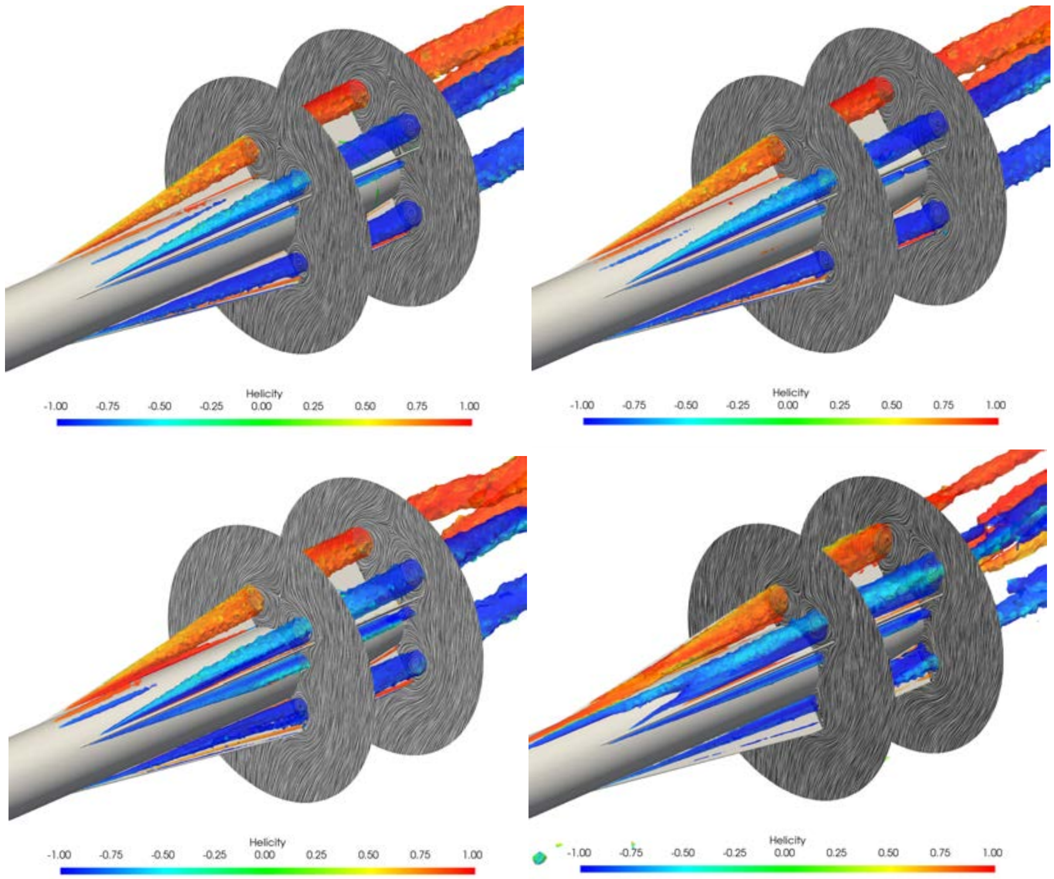

Fig. 7 Isosurfaces of scaled Q-criterion (value = 0.5) colored by normalized helicity and LIC representation of velocity vector on axial slices at $x/D = 8.38$ and $x/D = 10.0$, $\alpha_t = 12°$, and $M = 0.7$ (top left), 1.1 (top right), 2.0 (bottom left), and 4.0 (bottom right)

The vortex structures are visualized via axial cut planes of normalized axial vorticity, $\omega D/U_\infty$, in Fig. 8 where the progression of the vortex structures can be observed a little clearer. Up to $M = 2.0$, the symmetric leeside body vortices progress between the fins and then merge with the primary fin vortices. At $M = 4.0$, the larger body vortices appear to merge earlier with the fin vortices. In addition, the intensity of these vortex structures is less than at the lower Mach numbers, evidenced by the noticeably lower normalized vorticity level across the vortex core at downstream locations. At $x/D = 9.0$, the peak normalized vorticity in the vortex core was found to be 2.7, 3.9, 4.8, and 3.9 for $M = 0.7$, 1.1, 2.0, and 4.0, respectively. Although the peak values were similar at $M = 1.1$ and 4.0, the region of high vorticity was much smaller at the higher Mach number, with the vortex being more diffuse, as indicated in Fig. 8. The decrease in vortex structure strength with increasing Mach number, influenced by compressibility effects, was attributed to the decreased lateral load effects with roll orientation previously observed.[1,2,5] The primary vortex structures are also shown in Fig. 9, which shows the LIC representation of the velocity vector on four axial cut planes colored by normalized total pressure, P_0/P_{0_∞}, as viewed from the rear of the projectile. The size of the symmetric body vortices before entering the region between the fins is observed at $x/D = 4.0$, where they increase in size and intensity (lower local total pressure) with increasing Mach number. At $x/D = 5.0$, the separate symmetric body vortices and primary upper fin vortices can still be observed up to $M = 2.0$. However, at $M = 4.0$ these vortex structures have already merged at this location. At the last two axial locations, the progression of the other vortex structures is observed, notably the inward movement of the lower fin primary vortices moving inward at $M = 4.0$.

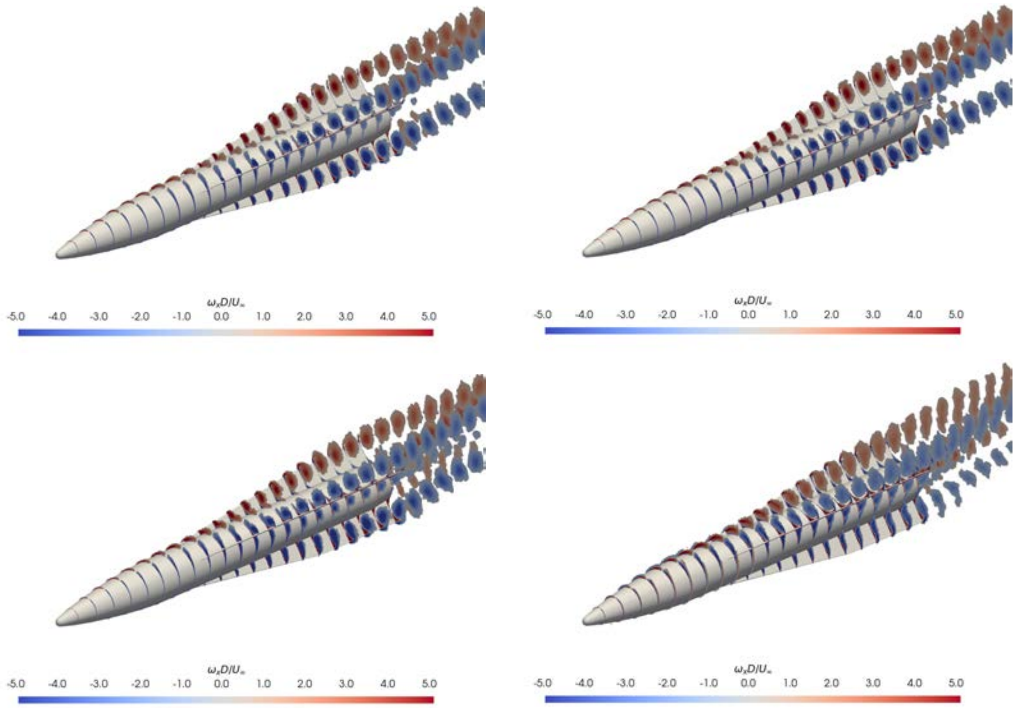

Fig. 8 Normalized axial vorticity on cross planes for $\alpha = 12°$, and $M = 0.7$ (top left), 1.1 (top right), 2.0 (bottom left), and 4.0 (bottom right)

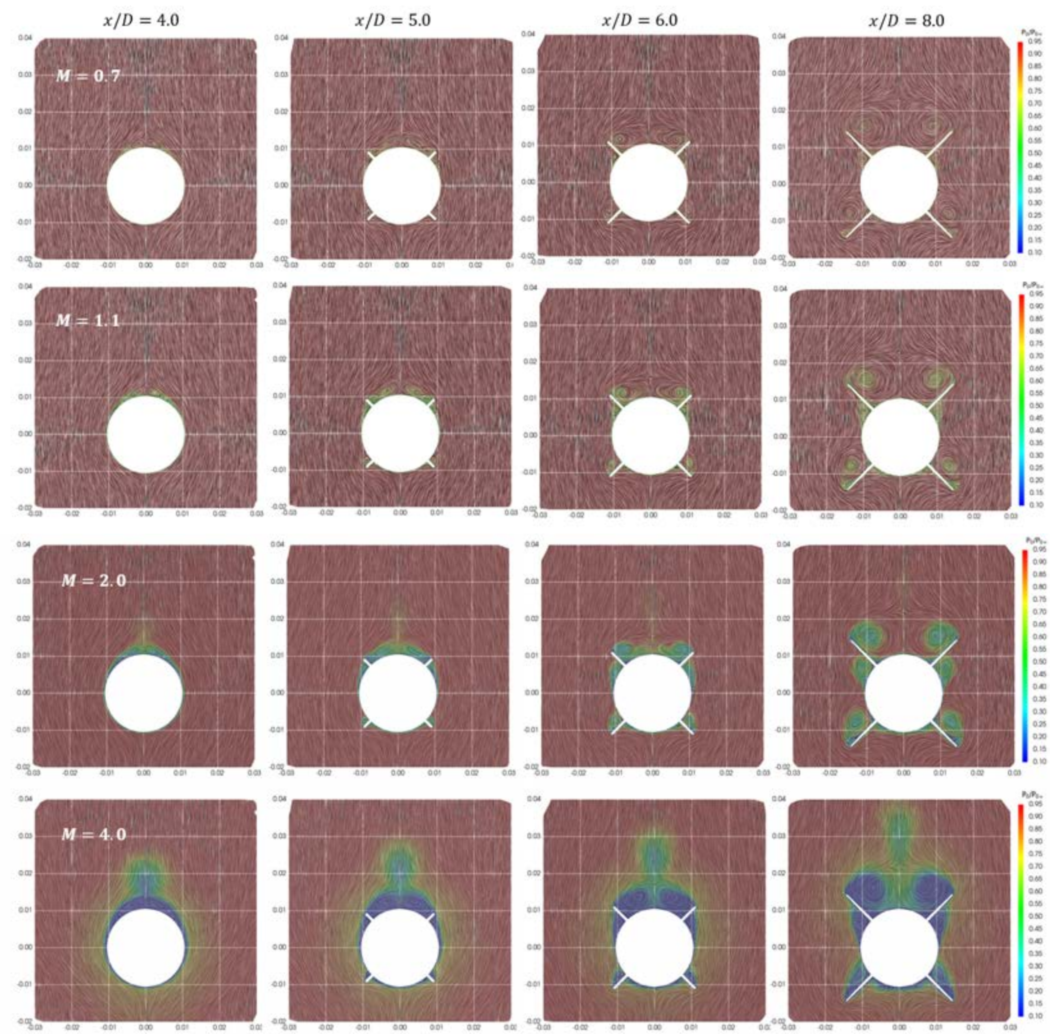

Fig. 9 LIC representation of velocity vector on axial slices at $x/D = 4$, 5, 6, and 8 colored by normalized total pressure for $\alpha_t = 12°$ and $M = 0.7$, 1.1, 2.0, and 4.0 (view from rear)

The surface flow patterns on the projectile at Mach 2 and $\alpha_t = 12°$ as viewed from the top, along the upper port fin, and from the port side are shown in Fig. 10, which compares the WT and CFD predictions. The surface is also colored using skin friction coefficient magnitude to highlight the surface flow. The CFD predicted flow structures generally compare well to that shown in the experimental oil flow. Separations and reattachment patterns near the fin tip and root are observed in both, as are those on the cylindrical body, which are due to the primary vortex structures. The port side view (bottom image) shows the most complex structure on the cylindrical body due to the interactions from both the leeward and windward fins. The general shape of the flow patterns is similar, but the experimental surface flow extends a bit closer to the windward (lower) fin root.

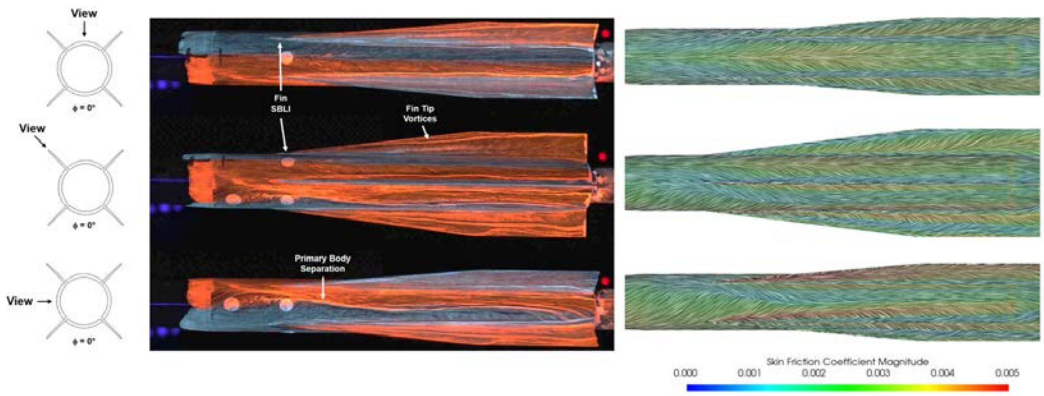

Fig. 10 Top (top), upper port fin (middle), and port side (bottom) views of WT surface oil-flow visualization (left) and CFD surface LIC oil-flow representation colored by skin friction coefficient magnitude, $M = 2$, $\alpha_t = 12°$

The CFD-predicted surface flow structures for the four Mach numbers are compared in Fig. 11 for the same three views shown in Fig. 10. There is almost no difference on the top section between Mach 0.7 and 1.1 and small differences along the top port fin and port side views. As the Mach number increases, the flow structures along the top of the cylinder body become more defined as the leeside vortex structures increase in size and are located closer to the body as they progress downstream (see Fig. 9). The effect of the vortices along the fin root are also more defined as secondary vortex structures have formed. At Mach 4, the effect of the symmetric vortices emanating from the ogive-cylinder junction appear to enhance this effect.

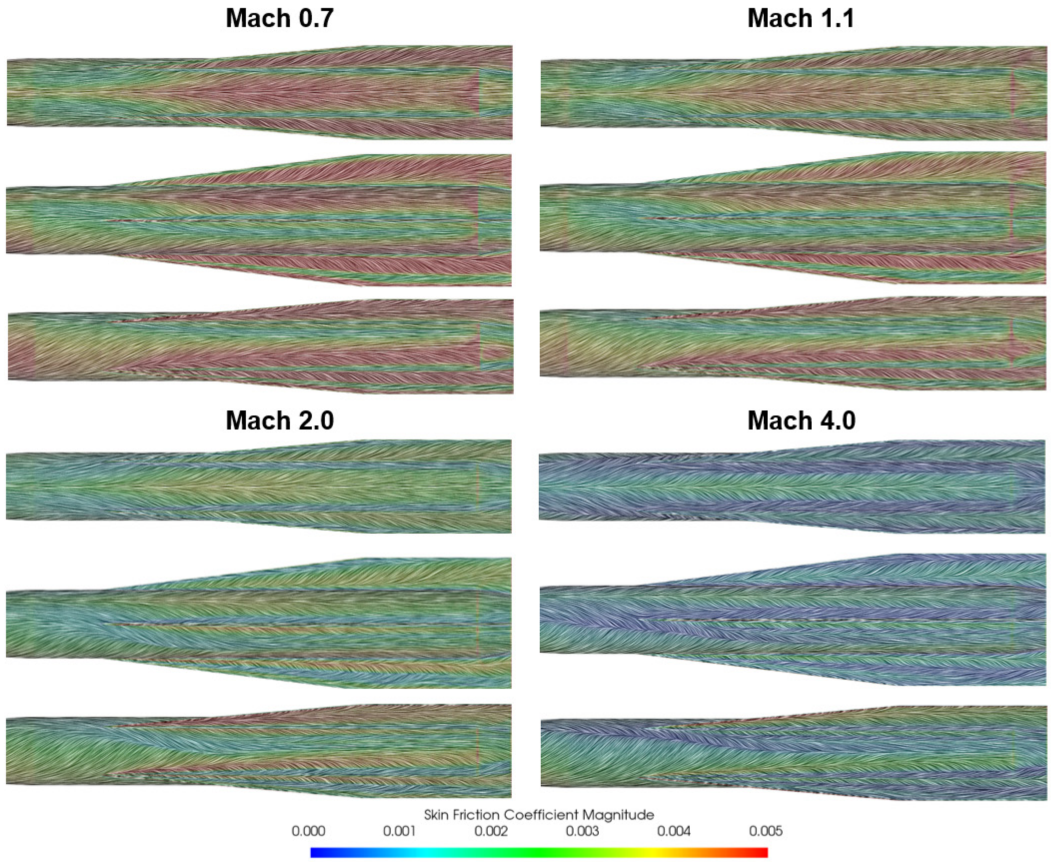

Fig. 11 Top, upper port fin, and port side views of CFD LIC oil-flow representation colored by skin friction coefficient magnitude at $\alpha_t = 12°$

4.2 Additional Analysis at $M = 2.0$

The pressure distribution on the projectile surface was analyzed by Pokela et al.[5] and those results are compared to the CFD-predicted surface pressure distribution in Figs. 12 and 13 for port side and top views, respectively at $\alpha_t = 6°$ and 12°. Qualitatively, the overall surface pressure distribution is predicted well. On the port side view, the pressure is overpredicted on the underside of the upper fin at both angles of incidence while the predicted pressure appears more uniform on the body at $\alpha_t = 6°$ than the WT PSP results indicate. At $\alpha_t = 12°$, the predicted pressure distribution on the port side of the body compares very well in structure with the WT PSP results. The predicted pressure distribution is again overpredicted on the leeside of the bottom fin. On the top view, Fig. 13, the predicted pressure distribution is again more uniform on the body at $\alpha_t = 6°$ and slightly overpredicted than observed in the WT PSP results. At $\alpha_t = 12°$, the predicted shape of the pressure distribution is very close to the WT PSP results but again slightly overpredicted. At both angles of incidence, the predicted pressure is overpredicted on the fins but the shape of the distribution is very similar.

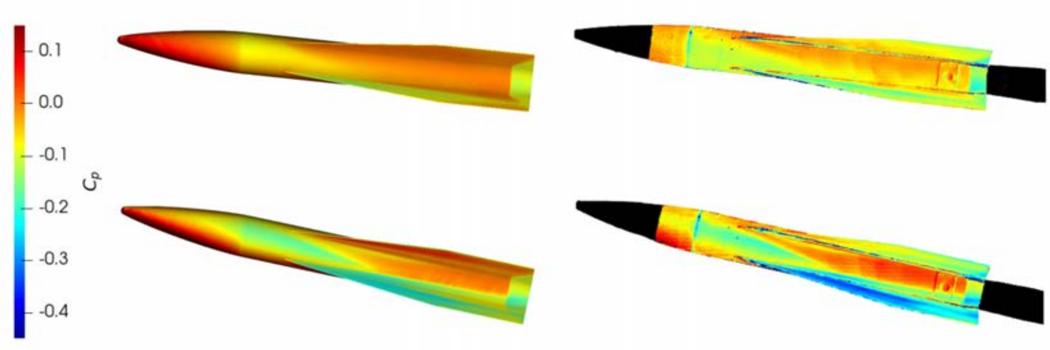

Fig. 12 Pressure coefficient on port side view of model surface from CFD (left) and acquired from WT PSP (right) at $\alpha_t = 6°$ (top) and $\alpha_t = 12°$ (bottom) and $M = 2.0$

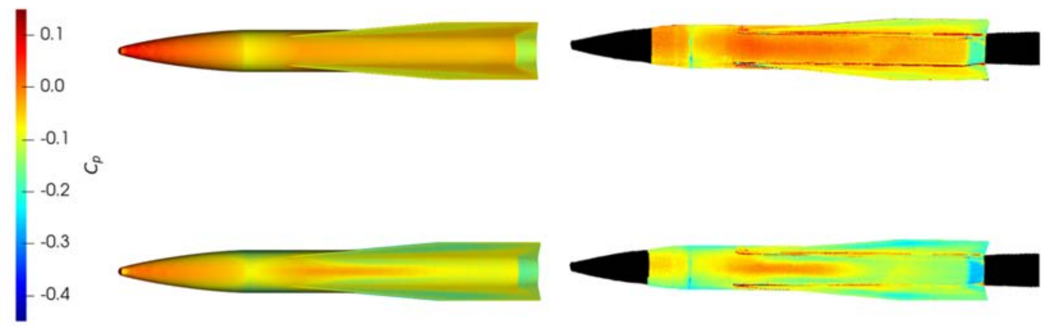

Fig. 13 Pressure coefficient on leeward side of model surface from CFD (left) and acquired from WT PSP (right) at $\alpha_t = 6°$ (top) and $\alpha_t = 12°$ (bottom) and $M = 2.0$

The predicted and WT PSP pressure distributions are compared quantitatively in Fig. 14 along axial profiles on the port side of the model as indicated at the top of the figure. The predicted results for several turbulence models are shown in the figure. As identified in the surface pressure distribution plots, the predicted pressure is overpredicted on the underside of the upper fin (port side location “a”). At port side location “b,” the axial distribution and pressure values are predicted very well at both incidence angles. At $\alpha_t = 6°$, the predicted profiles are very similar at locations “c” and “d,” indicating the azimuthal uniformity also observed in Fig. 12, while the WT PSP profiles show a similar distribution but slightly lower values at location “d.” At the higher angle of incidence, the trends in the profiles at these two locations are well predicted and the pressures compare very well at location “c.” The surface pressure is again overpredicted by a larger margin on the leeside surface of the lower fin—location “e.” The largest differences in predicted and measured pressure values are in regions in proximity to the major vortex structures (e.g., locations “a,” “d,” and “e”), supporting the importance of accurately predicting these structures. In addition to predictions using the baseline Menter SST turbulence model, predictions using the SA model and the two rotation-correction modifications are also shown. The predicted pressure profiles overlay for all cases except location “e,” which undergoes the largest suction pressure due to the leeside separation on the fin. The SARC rotation-corrected model shows the closest prediction to the WT PSP from about $x/D = 8.2$–9.5; however, the SAR rotation-corrected model shows the largest overprediction. The SST model shows very little effect of the rotation-correction modification, grouped near the SAR prediction. The overpredicted surface pressure, especially above the fin locations, may indicate that the predicted vortex structures have lower intensity than in the experiment due to numerical diffusion. The rotation-correction modifications are supposed to alleviate this effect by reducing the overprediction of turbulent kinetic energy in the vortex core but appears to only be significant for the SARC model. Further investigations using a more resolved mesh and unsteady, hybrid RANS/large-eddy simulation (LES) simulations are planned to determine if improved predictions can be obtained.

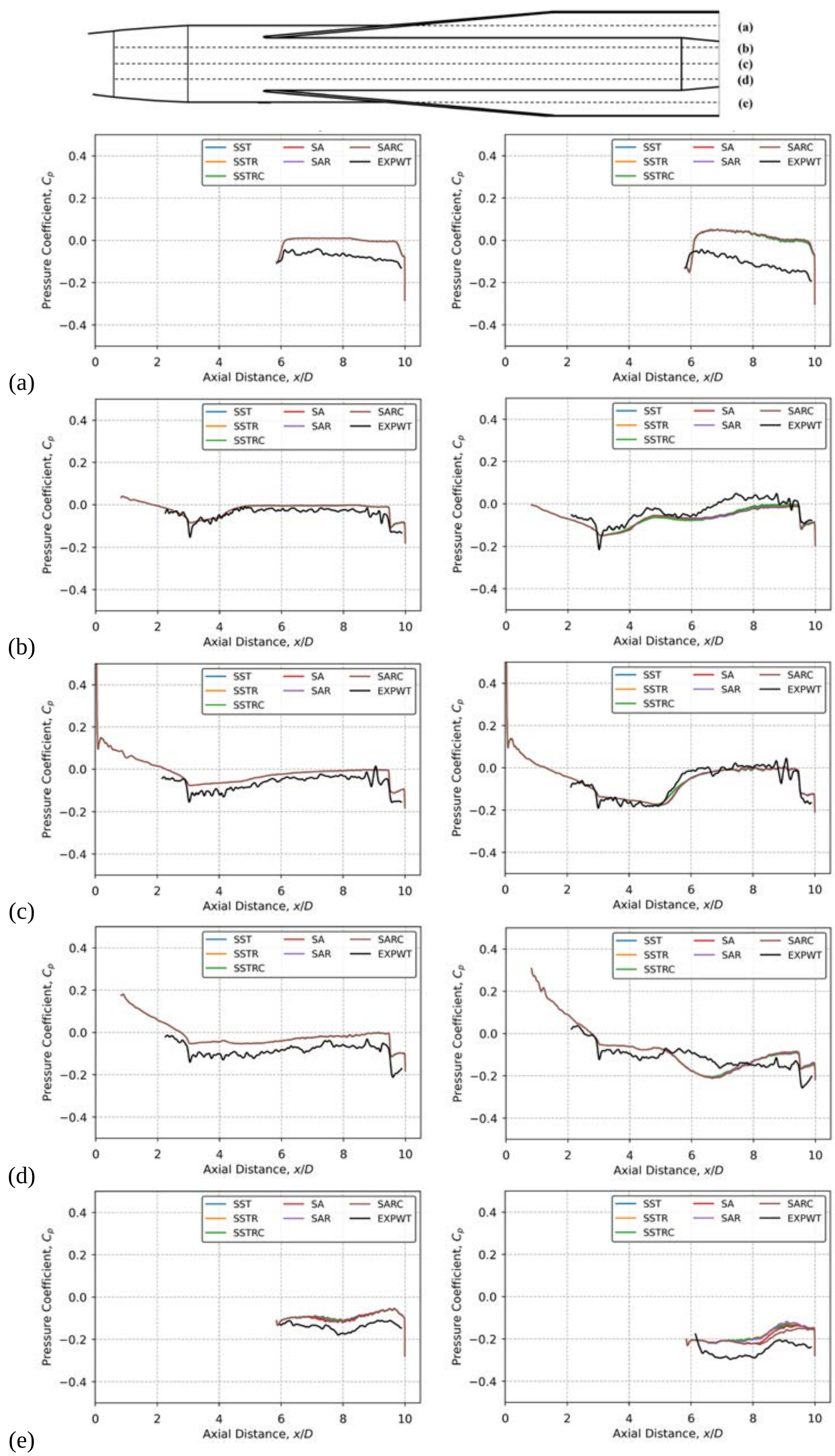

Fig. 14 Pressure coefficient profiles extracted from port side of model for $\alpha_t = 6°$ (left) and $\alpha_t = 12°$ (right) along locations "a" through "e"

The predicted and WT PSP pressure distributions on the leeward (top) side of the model are compared in Fig. 15. The predicted pressures are again overpredicted along the fin, location "a," but no effects of turbulence model or rotation-correction modification is observed. The predicted pressure is again more uniform on the body (locations "b" and "c") between the fins at $\alpha_t = 6°$ and slightly underpredicted compared to the WT PSP for $3 \leq x/D \leq 6$. The pressure is predicted very well at the location "b" at the higher angle of incidence, but slightly overpredicted for $6 \leq x/D \leq 9.5$. At location "c," the pressure is well predicted at $\alpha_t = 6°$ but is again overpredicted at the higher incidence angle. The difference in the pressure distribution at this location and the higher incidence angle is likely due to the accuracy of the prediction of the counter-rotating vortex pair traveling downstream between the leeward fins.

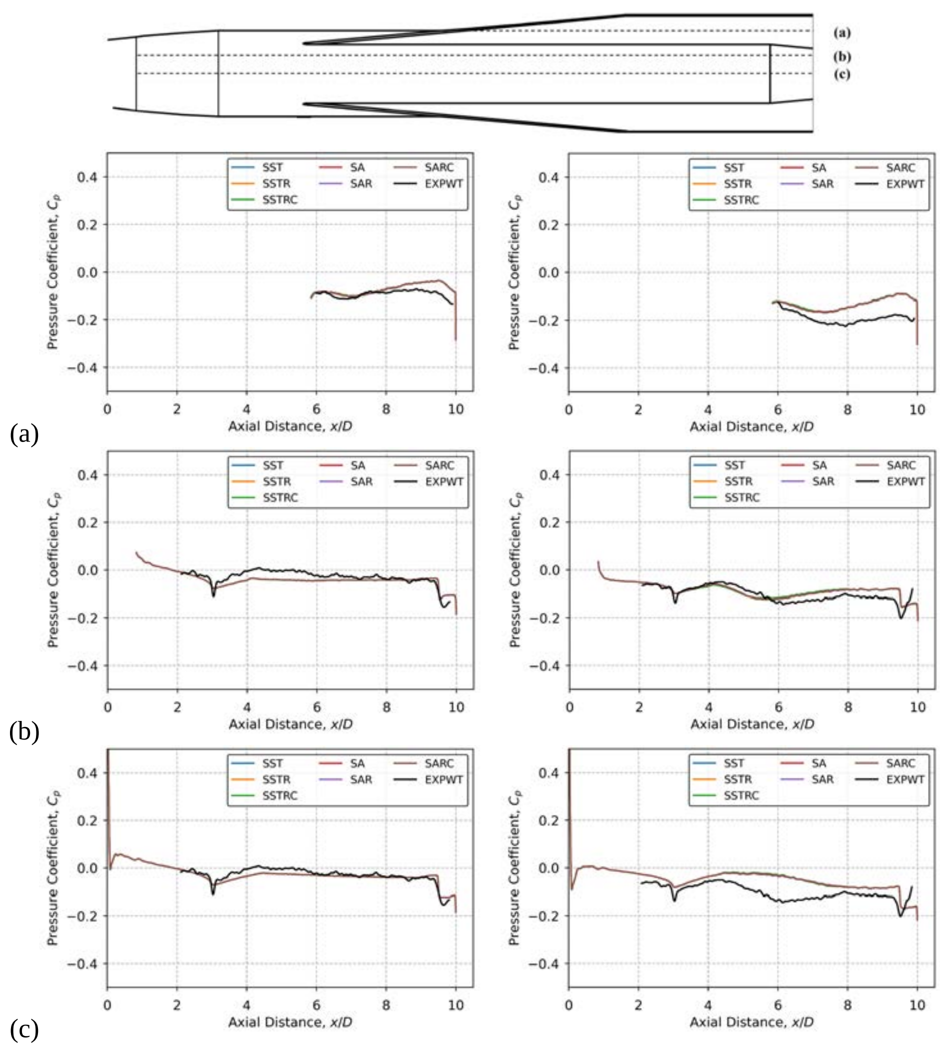

Fig. 15 Pressure coefficient profiles extracted from leeward side of model for $\alpha_t = 6°$ (left) and $\alpha_t = 12°$ (right) along locations "a" through "c"

The effect of the rotation correction on the vortex structures is shown in Fig. 16 using contours of turbulent eddy viscosity ratio, μ_t/μ, to indicate the level of turbulence predicted in the vortex cores. The SST-based models are shown in the upper part of the figure and the SA-based models are shown in the lower part. The rotation-correction modification reduces the overprediction of turbulence in the vortex core and the “RC” corrected flow fields show lower turbulent eddy viscosity levels in the vortex cores (note the log scale). However, the effect on the predicted pressure profiles was only observed on the lower fin surface (Fig. 14e). A similar investigation of all six turbulence model variants will be performed on a high-resolution mesh, but the “RC” correction should likely be used as a default for flows with vortex structures such as these.

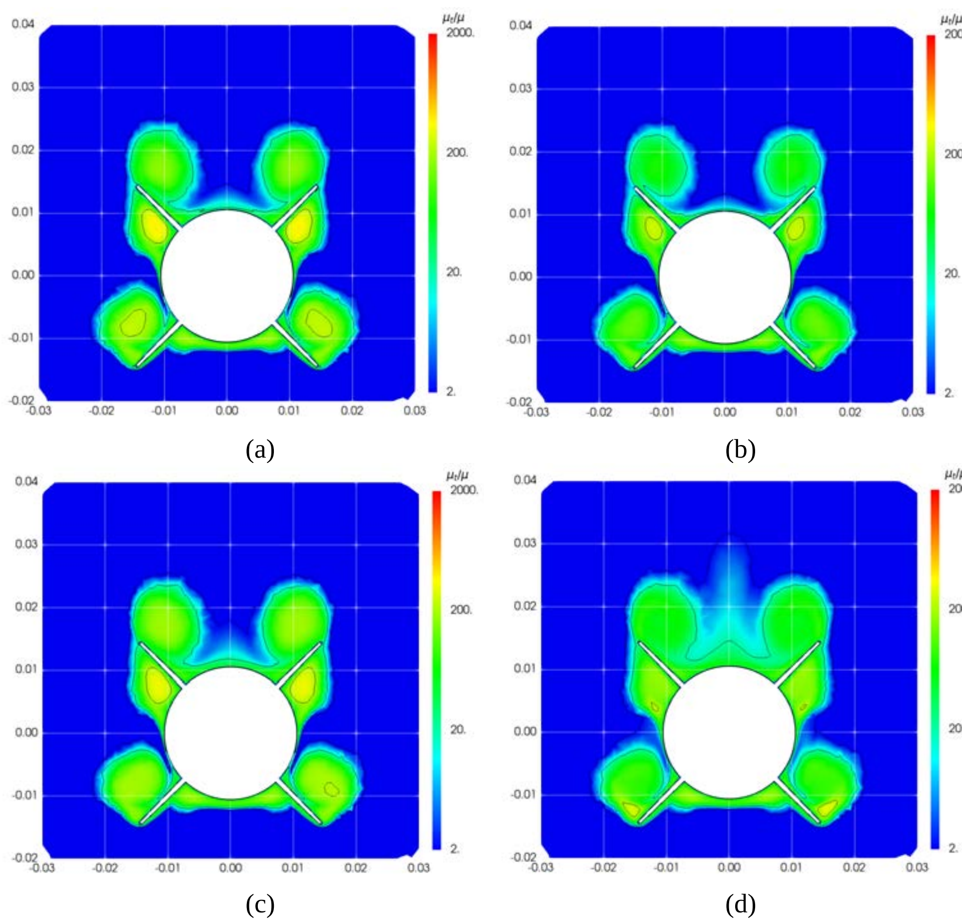

Fig. 16 Contours of turbulent eddy viscosity ratio on axial plane at $x/D = 9.0$ at $\alpha_t = 12°$ and $M = 2.0$ using the SST (a), SSTRC (b), SA (c), and SARC (d) turbulence models

Finally, profiles of skin friction coefficient magnitude, C_f, are shown for the port side and leeward side model surfaces in Figs. 17 and 18, respectively. Wind tunnel data is not available for skin friction values. Turbulence model variant has little effect except near both sides of the upper fin root (locations “b”). The differences are primarily between the SST-based models and the SA-based models rather than rotation-correction modification. The reason for this difference is difficult to determine from cross-plane visualization such as in Fig. 16, but there are slight differences in the vortex structure and intensity.

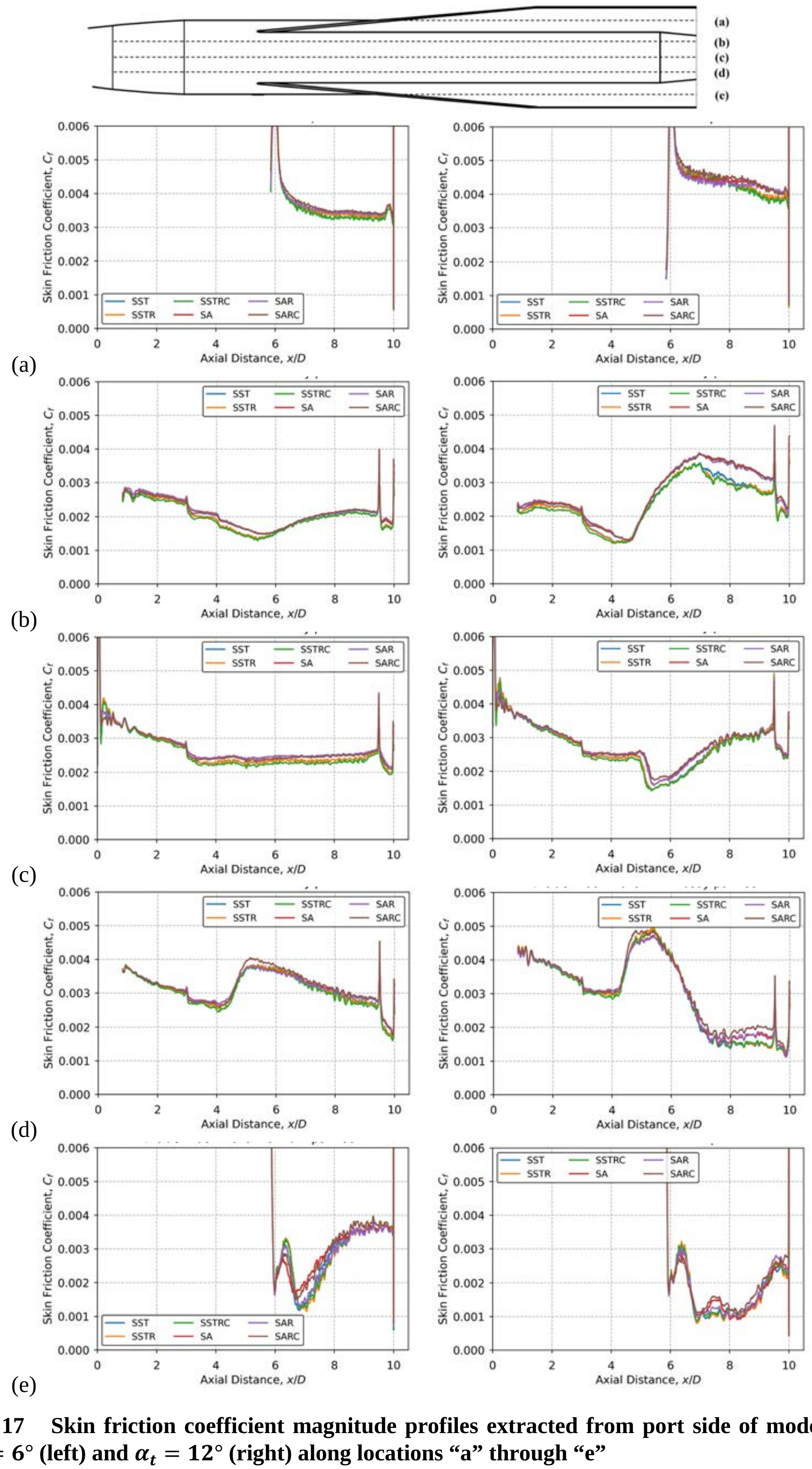

Fig. 17 Skin friction coefficient magnitude profiles extracted from port side of model for $\alpha_t = 6°$ (left) and $\alpha_t = 12°$ (right) along locations "a" through "e"

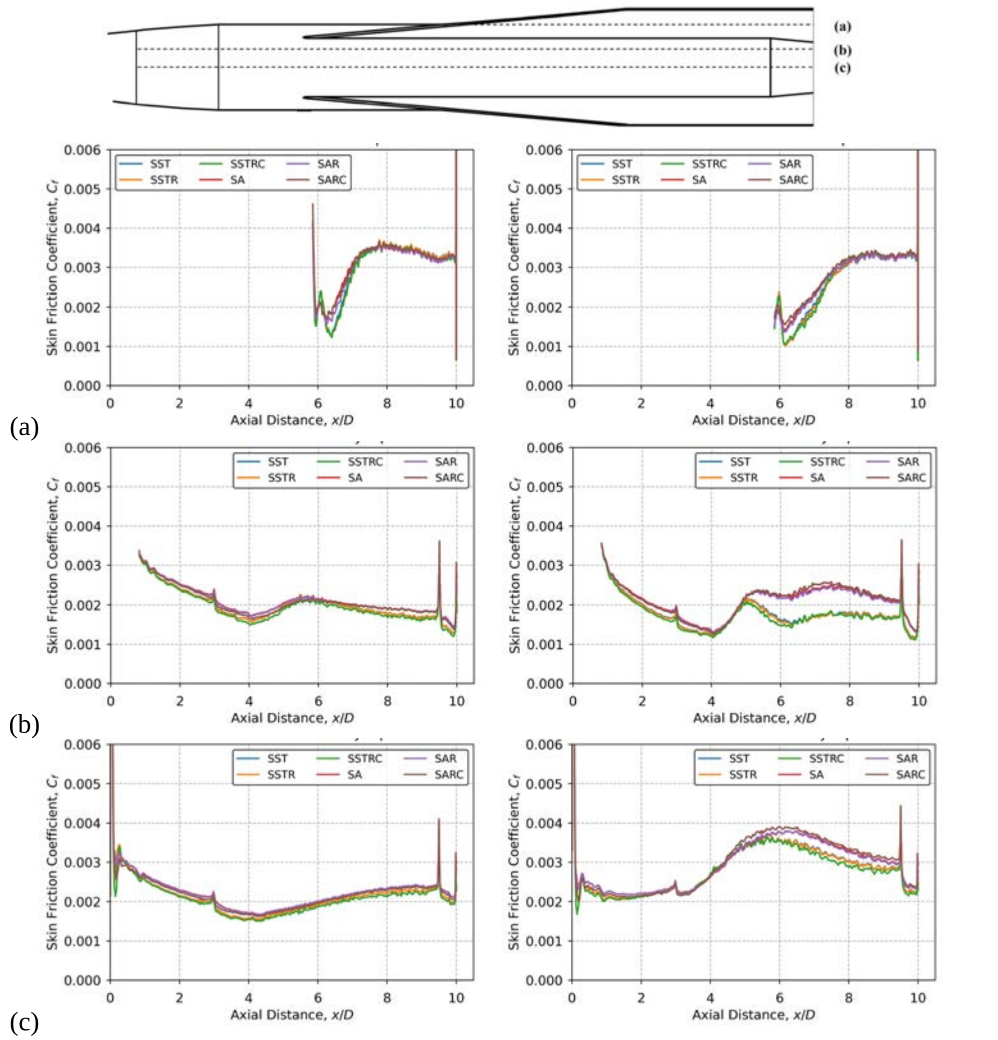

Fig. 18 Skin friction coefficient magnitude profiles extracted from leeward side of model for $\alpha_t = 6°$ (left) and $\alpha_t = 12°$ (right) along locations "a" through "c"

5. Conclusion and Future Plans

A combined experimental and numerical study was conducted on a generic symmetric projectile configuration with four high-sweep, low-aspect-ratio fins. The study is a continuation of previous investigations of this configuration with the goal of obtaining enhanced flow field scientific visualizations and analyses to compare to available WT flow diagnostics, including high-speed shadowgraphy, oil-flow visualization, and fast-response PSP. Predicted drag and normal force coefficients compared well to the WT results. The predicted pitching moment coefficient about the nose compared well to the WT results but the predicted error of the pitching moment about the c.g. was larger than desired for a configuration with a small static margin (distance between pitching moment center of pressure and c.g.). The predicted off-body flow structures (vortices and shock waves) compared very well with those observed on the WT model. The predicted surface streak lines and pressure distribution also compared well with the WT results. Comparison of predicted and WT surface pressure distributions shows that the simulations tended to overpredict the surface pressure at most locations, primarily on the leeward surfaces of the fins. The effect of the turbulence model and rotation-correction modifications showed little effect on the surface pressure distribution except on the leeward surface of the lower fin, where the SARC model showed an improved comparison with the WT result on the leeward surface of the upper fin.

Additional investigations are planned involving using a higher-resolution mesh and adaptive mesh refinement to determine if numerical diffusion of the vortex structures can be improved. Additional analyses will also include further analysis of the predicted shock structures and time-accurate, scale-resolving simulations to investigate unsteadiness of the flow. Additional WT investigations at Mach 2.0 will include particle image velocimetry, which will allow direct comparison of the off-body flow field, and tests with the model in a nonsymmetric roll orientation of $\phi = -22.5°$. The latter tests will investigate how the nonsymmetric flow structures interact to generate asymmetric aerodynamic loading that has been observed.[1–4]

6. References

1. Pokela R, Kumar R, Vasile JD. Experimental and computational aerodynamic characterization of a generic high-speed projectile configuration. AIAA Aviation Forum; 2021 Aug 2–6; virtual event. AIAA Paper 2021-2607.

2. Pokela R, Kumar R, Vasile JD, DeSpirito J. Aerodynamic characterization of a generic high-speed projectile configuration. AIAA J Spacecr Rockets; Forthcoming.

3. Vasile JD, Bryson JT, Sahu J, Paul JL, Gruenwald BC. Aerodynamic dataset generation of a long-range projectile. DEVCOM Army Research Laboratory (US); 2020 Aug. Report No.: ARL-TR-9019.

4. Vasile JD, Sahu J. Roll orientation–dependent aerodynamics of a long-range projectile. DEVCOM Army Research Laboratory (US). 2020 Aug. Report No.: ARL-TR-9017.

5. Pokela R, Gustavsson J, Kumar R. Surface pressure measurements on an axisymmetric body with fins using pressure sensitive paint. AIAA Aviation Forum; 2023 June 12–16; San Diego, CA. AIAA Paper 2023-3677.

6. Van Every DH, Best S, Strike JA, Kumar R. Commissioning of a polysonic wind tunnel at the Florida State University. 53rd AIAA Aerospace Sciences Meeting; 2015 Jan 5–9; Kissimmee, FL. AIAA Paper 2015-2015.

7. AIAA G-129-2012(2017). Guide: nomenclature and axis systems for aerodynamic wind tunnel testing. American Institute of Aeronautics and Astronautics, Inc.; 2012. doi.org/10.2514/4.869150.001.

8. Houlden H, Favaregh A, Hemsch M. Quantification of the uncertainties for the Ares I A106 Ascent aerodynamic database. 27th AIAA Aerodynamic Measurement Technology and Ground Testing Conference; 2010 June 28–July 1; Chicago, IL. AIAA Paper 2010-4926.

9. Favaregh AL, Houlden H, Pinier JT, Hemsch MJ. Space launch system aerodynamic database uncertainty quantification methodologies. 54th AIAA Aerospace Sciences Meeting; 2016 Jan 4–8; San Diego, CA. AIAA Paper 2016-0795.

10. McDaniel DR, Tuckey TR. HPCMP CREATE™-AV Kestrel: new capabilities and future directions. AIAA SciTech 2019 Forum; 2019 Jan 7–11; San Diego, CA. AIAA Paper 2019-0840. doi.org/10.2514/6.2019-0840.

11. McDaniel DR, Nichols RH, Eymann TA, Starr RE, Morton SA. Accuracy and performance improvements to Kestrel's near-body flow solver. AIAA SciTech 2016 Forum; 2016 Jan 4–8; San Diego, CA. AIAA Paper 2016-1051. doi.org/10.2514/6.2016-1051.

12. Nishikawa H, Nakashima Y, Watanabe N. Effects of high-frequency damping on iterative convergence of implicit viscous solver. J Comp Phys. 2017;348:66–81. doi.org/10.1016/j.jcp.2017.07.021.

13. Menter FR. Two-equation eddy-viscosity turbulence models for engineering applications. AIAA J. 1994;32(8):1598–1605. doi.org/10.2514/3.12149.

14. Nichols RH. Modification of the turbulence models in the CREATE™-AV Kestrel flow solvers for high speed flows. AIAA SciTech 2022 Forum; 2022 Jan 3–7; San Diego, CA. AIAA Paper 2022-1174. doi.org/10.2514/6.2022-1174.

15. Spalart P, Allmaras S. A one-equation turbulence model for aerodynamic flows. 30th Aerospace Sciences Meeting and Exhibit; 1992 Jan 6–9; Reno, NV. AIAA Paper 1992-0439.

16. Dacles-Mariani J, Zilliac G, Chow J, Bradshaw P. Numerical/experimental study of a wingtip vortex in the near field. AIAA J. 1995;33(9):1561–1568.

17. Shur ML, Spalart PR, Strelets MK, Travin AK. A hybrid RANS-LES approach with delayed-DES and wall-modelled LES capabilities. Int J Heat Fluid Flow. 2008;29(6):1638–1649.

18. Mestreau E, Aubry R, Dey S, Richardson M. CREATE-MG capstone: design, architecture & feature modelling improvements. AIAA SciTech 2019 Forum; 2019 Jan 7–11, San Diego, CA. AIAA Paper 2019-1716.

19. Ahrens JP, Geveci B, Law CC. ParaView: an end-user tool for large data visualization. Visualization handbook. Elsevier; 2005 Jan. p. 717–731.

List of Symbols, Abbreviations, and Acronyms

AIAA	American Institute of Aeronautics and Astronautics
ARL	Army Research Laboratory
c.g.	center of gravity
CFD	computational fluid dynamics
CREATE	Computational Research and Engineering Acquisition Tools and Environments
DEVCOM	US Army Combat Capabilities Development Command
DOD	Department of Defense
FAMU	Florida A&M University
FSU	Florida State University
HLLE	Harten–Lax–van Leer–Einfeldt
HPCPMP	DOD High-Performance Computing Modernization Program
KCFD	Kestrel computational fluid dynamics
LED	light-emitting diode
LES	large-eddy simulation
LIC	line integral convolution
MRP	moment reference point, calibers
PSP	pressure-sensitive paint
PSWT	polysonic wind tunnel
PtTFPP	Pt(II) meso-tetra (pentafluorophenyl) porphine
RANS	Reynolds-averaged Navier-Stokes
RMS	root-mean-squared
SA	Spalart–Allmaras
SAR	Spalart–Allmaras with rotation correction
SARC	Spalart–Allmaras with rotation and curvature correction
SBLI	shock-boundary layer interaction

SST	Shear Stress Transport
SSTR	Shear Stress Transport with rotation correction
SSTRC	Shear Stress Transport with rotation and curvature correction
UV	ultraviolet
WT	wind tunnel

Symbols

α_t	angle of incidence, °
C_f	skin friction coefficient
C_D	drag coefficient
C_N	normal force coefficient
C_p	pressure coefficient
C_{PM}	pitch moment coefficient
$C_{PM_{cg}}$	pitch moment coefficient about projectile c.g.
$C_{PM_{nose}}$	pitch moment coefficient about projectile nose
C_{SF}	side force coefficient
D	diameter
M	Mach number
μ_t	turbulent eddy viscosity, m^2/s
μ	dynamic viscosity, $N\text{-}s/m^2$
P_0	total pressure, Pa
$P_{0\infty}$	freestream total pressure, Pa
ϕ	roll angle, °
q_∞	freestream dynamic pressure, Pa
ρ	density, kg/m^3
S	model cross-sectional area, m^2
U_∞	freestream velocity, m/s

$\boldsymbol{\omega}$	vorticity vector, 1/s
x, y, z	body axes in the axial, lateral, and longitudinal direction
x_{cg}	center of gravity location, caliber
x_{cp}	center of pressure location, calibers